Spectroscopy of the archetype colliding-wind binary WR 140 during the 2009 January periastron passage

R. Fahed, A. F. J. Moffat, J. Zorec, T. Eversberg, A. N. Chené, M. F. Corcoran, S. M. Dougherty, Y. Frémat, J. H. Knapen, R. Leadbeater, et al.

Monthly Notices
of the
ROYAL ASTRONOMICAL SOCIETY

Mon. Not. R. Astron. Soc. **418,** 2–13 (2011) doi:10.1111/j.1365-2966.2011.19035.x

Spectroscopy of the archetype colliding-wind binary WR 140 during the 2009 January periastron passage

R. Fahed,[1⋆]† A. F. J. Moffat,[1⋆] J. Zorec,[2] T. Eversberg,[3⋆] A. N. Chené,[4,5,6] F. Alves,[⋆] W. Arnold,[⋆] T. Bergmann,[⋆] M. F. Corcoran,[7] N. G. Correia Viegas,[⋆] S. M. Dougherty,[8] A. Fernando,[⋆] Y. Frémat,[9] L. F. Gouveia Carreira,[⋆] T. Hunger,[⋆] J. H. Knapen,[10,11⋆] R. Leadbeater,[12⋆] F. Marques Dias,[⋆] C. Martayan,[13] T. Morel,[14⋆] J. M. Pittard,[15] A. M. T. Pollock,[16] G. Rauw,[14⋆] N. Reinecke,[⋆] J. Ribeiro,[⋆] N. Romeo,[⋆] J. R. Sánchez-Gallego,[10,11⋆] E. M. dos Santos,[⋆] L. Schanne,[⋆] O. Stahl,[⋆] Ba. Stober,[⋆] Be. Stober,[⋆] K. Vollmann[⋆] and P. M. Williams[17]

[1]*Département de physique, Université de Montréal, CP 6128, Succ. C.-V., Montréal, QC H3C 3J7, and Centre de Recherche en Astrophysique du Québec, Canada*
[2]*Institut d'Astrophysique de Paris, UMR7095 CNRS, Université Pierre et Marie Curie, 98bis bd. Arago F-75014 Paris, France*
[3]*Schnörringen Telescope Science Institute, Waldbröl, Germany*
[4]*Canadian Gemini Office, HIA/NRC of Canada, 5071 West Saanich Road, Victoria, BC V9E 2E7, Canada*
[5]*Departamento de Astronomía, Facultad de Ciencias Físicas y Matemáticas, Av. Esteban Iturra s/n Barrio Universitario, Universidad de Concepción, Casilla 160-C, Concepción, Chile*
[6]*Departamento de Física y Astronomía, Facultad de Ciencias, Universidad de Valparaíso, Av. Gran Bretaña 1111, Playa Ancha, Casilla 5030, Valparaíso, Chile*
[7]*CRESST and X-ray Astrophysics Laboratory, NASA/GSFC, Greenbelt, MD 20771, USA; Universities Space Research Association, 10211 Wisconsin Circle, Suite 500, Columbia, MD 21044, USA*
[8]*National Research Council, Herzberg Institute of Astrophysics, Dominion Radio Astrophysical Observatory, PO Box 248, Penticton, BC V2A 6J9, Canada*
[9]*Royal Observatory of Belgium, 3 Av. circulaire, B-1180 Bruxelles, Belgium*
[10]*Instituto de Astrofísica de Canarias, E-38205 La Laguna, Tenerife, Spain*
[11]*Departamento de Astrofísica, Universidad de La Laguna, E-38200 La Laguna, Tenerife, Spain*
[12]*Three Hills Observatory, The Birches, CA7 1JF*
[13]*European Organization for Astronomical Research in the Southern Hemisphere, Alonso de Cordova 3107, Vitacura, Santiago de Chile, Chile*
[14]*Institut d'Astrophysique et de Géophysique, Université de Liège, 17 Allée du 6 Aout, B-4000 Liège 1 (Sart Tilman), Belgium*
[15]*School of Physics and Astronomy, University of Leeds, Woodhouse Lane, Leeds LS2 9JT*
[16]*European Space Agency XMM–Newton Science Operations Centre, Apartado 78, 28691 Villanueva de la Cañada, Spain*
[17]*Royal Observatory, Blackford Hill, Edinburgh EH9 3HJ*

Accepted 2011 May 6. Received 2011 May 5; in original form 2011 March 7

ABSTRACT

We present the results from the spectroscopic monitoring of WR 140 (WC7pd + O5.5fc) during its latest periastron passage in 2009 January. The observational campaign consisted of a constructive collaboration between amateur and professional astronomers. It took place at six locations, including Teide Observatory, Observatoire de Haute Provence, Dominion Astrophysical Observatory and Observatoire du Mont Mégantic. WR 140 is known as the archetype of colliding-wind binaries and it has a relatively long period ($\simeq$8 yr) and high eccentricity ($\simeq$0.9). We provide updated values for the orbital parameters, new estimates for the WR and O star masses and new constraints on the mass-loss rates and colliding-wind geometry.

Key words: binaries: general – stars: fundamental parameters – stars: winds, outflows – stars: Wolf–Rayet.

1 INTRODUCTION

Binary systems provide the least model-dependent way to secure measurements of stellar masses. Understanding binary systems is therefore of paramount importance for many problems in stellar astrophysics. In the case of massive stars and most particularly

⋆Mons Pro-Am collaboration.
†E-mail: fahed@astro.umontreal.ca

WR+O systems, the strong, fast winds of the two stars will interact with each other along a shock surface, giving rise to an excess emission in a range of wavelengths going from radio to X-rays, possibly even γ-rays (Moffat & St-Louis 2002). Understanding the underlying physics of this phenomenon gives us access to additional parameters of the system, such as the wind momentum ratio and the orbital inclination.

Among these colliding-wind systems, WR 140 is considered as the archetype. WR 140 is a WC7pd + O4–5 system with a large eccentricity ($e = 0.88$) and long period ($P = 7.94$yr) (Marchenko et al. 2003, hereafter M03). It is also the brightest Wolf–Rayet (WR) star in the Northern hemisphere (Cygnus) with a visual magnitude of 6.9. It was first suggested as a spectroscopic binary in 1924 (Plaskett 1924). However, searches for radial velocities (RVs) were unsuccessful until a period was found in infrared photometry (Williams et al. 1987) and a first spectroscopic orbit in 1987 (Moffat et al. 1987). A spectroscopic campaign around periastron in 2001 revealed that the spectral changes as a result of the wind–wind collision were much faster than expected and therefore not sampled properly. New spectroscopic observations were thus requested in 2009 around periastron.

In this paper, we present our analysis of an international optical spectrometric campaign, which involved both professional and amateur astronomers at six locations. The campaign focuses on a short but crucial fraction of the orbit (four months) around the 2009 January periastron passage, during which the RVs vary most significantly.

In Section 2, we describe the multisite observational campaign and we present the different instruments used. We then devote Section 3 to the data reduction procedure. We also present the orbital solution deduced from the RV measurements of the two components in Section 4, and we look at what can be said about the spectral classification of the stars in Section 5, in particular the luminosity class of the O star. Finally, in Section 6, we discuss the analysis of the excess emission induced by the colliding-wind region (CWR).

2 OBSERVATIONS

2.1 Pro-Am campaign

One of the highlights of this observational campaign is that it consisted of a constructive collaboration between amateur and professional astronomers. Indeed, since the appearance of the first commercial spectrographs, such as those of the French company Shelyak, a small, but growing, community of amateurs is willing to involve themselves in scientific collaborations with professionals. The Be Star Spectra (BeSS) project of Be star spectroscopy, under the supervision of Coralie Neiner and François Cochard, is an example of such a collaboration (Neiner et al. 2007). See the websites of Amateur Astronomy Association (VDS; Germany)[1] and Astronomical Ring for Access to Spectroscopy (ARAS; France)[2] for further information about amateur groups involved in the Pro-Am collaboration. With progressive improvements, these projects are offering a serious alternative to traditional observational modes, especially for monitoring over long time-scales.

[1] http://spektroskopie.fg-vds.de/
[2] http://www.astrosurf.com/aras/

2.2 Data

Among the data collected through the Pro-Am collaboration, first we have the Mons project. Under the leadership of one of us (TE), a LHIRES III spectrograph was installed on a telescope previously owned by the University of Mons, Belgium, and nowadays used mainly for teaching purposes. This is a 50-cm telescope located at the Teide Observatory of the Instituto de Astrofísica de Canarias (IAC) in Tenerife. Four months of data were acquired with this instrumentation. Other amateurs contributed using their own personal instruments in Portugal (José Ribeiro), Germany (Berthold Stöber) and England (Robin Leadbeater at Three Hills Observatory[3]).

The rest of the data were obtained with the echelle spectrograph SOPHIE at the Observatoire de Haute Provence (OHP) and with more traditional single-grating long-slit spectrographs at the Dominion Astrophysical Observatory (DAO) and at the Observatoire du Mont-Megantic (OMM). We are primarily interested in the yellow spectral region ($\simeq$5500–6000 Å) where the main CWR-sensitive optical emission lines of C III 5696 Å and He I 5876 Å lie. A list of the data sets of the campaign is presented Table 1.

3 DATA REDUCTION

3.1 Pre-reduction

Each set of data was first pre-reduced in the standard way using the CCDPROC package in IRAF[4] and following the procedure described in 'A User's Guide to Reducing Slit Spectra with IRAF' by Massey, Valdes & Barnes (1992):[5] bias subtraction, normalized flat division and cosmic-ray removal using the routine COSMICRAYS. For the amateur spectra, the neon comparison lamps present only a few lines in the main yellow spectral range. The calibration exposures were thus overexposed to access the more numerous very faint neon lines, leading to a saturation of the fewer stronger lines. About 12 lines were used to compute the dispersion solution. In spite of this, the wavelength calibration was sufficiently accurate for our purpose. Where it was present, we used the interstellar sodium doublet at $\lambda\lambda$5890,5895 Å as a fine-tuning of the dispersion solution. This was done by applying a constant shift in wavelength to this solution in order to obtain the doublet at the right position. In the vast majority of cases, this shift is less than two pixels (it is always less than one pixel for the OHP data).

The echelle spectra were reduced using the automatic OHP reduction package adapted from the HARPS software of the Geneva Observatory. It includes a procedure to reconnect the orders of the echelle spectrum, thus leading to a single one-dimensional spectrum. However, this reconnection procedure is not perfect and a flux residual of variable amplitude centred around 5 per cent persists in the data. This defect was, for the most part, removed by using the fact that its shape was nearly constant. This shape was determined by dividing the spectra by each other, which nearly eliminated the stellar line contribution, and by fitting an appropriate analytical model using

[3] http://www.threehillsobservatory.co.uk/
[4] IRAF is the Image Reduction and Analysis Facility, a general purpose software system for the reduction and analysis of astronomical data. IRAF is written and supported by the IRAF programming group at the National Optical Astronomy Observatories (NOAO) in Tucson, AZ. The NOAO is operated by the Association of Universities for Research in Astronomy (AURA), Inc., under cooperative agreement with the National Science Foundation (http://iraf.noao.edu/).
[5] http://iraf.noao.edu/docs/spectra.html

Table 1. List of the different data sets in the 2009 campaign. Names marked with an asterisk are amateur astronomers/organizations equipped with their personal instrumentation. We also show the relative weight (= normalized $1/\sigma^2$, where σ is the dispersion around the fitted RV curve) used in the orbit fit.

Observatory	Dates	λλ (Å)	Recip. disp. (Å pixel^{-1})	Res. (pixels)	No. of spectra	Weight
Teide/Mons 50 cm	08.12.01–09.03.23	5530–6000	0.35	5–6	34	0.12
OHP/193 cm	08.12.12–09.03.23	3900–6800	0.01	15	63	0.49
DAO/120 cm	08.04.22–09.01.09	5350–5900	0.37	4.5	13	0.16
OMM/160 cm	09.07.05–09.08.08	4500–6000	0.63	2.6	18	0.09
Three Hills Obs.* (UK)	07.12.10–09.03.20	5600–6000	0.68	3.5	38	0.08
Berthold Stober* (Germany)	08.08.26–09.02.29	5500–6100	0.53	2–3	12	0.06

one polynomial per order of the echelle spectrograph (39 in total); these polynomials were then smoothly reconnected with each other. We finally modified all the spectra with this correction so that they best matched a non-affected single-grating spectrum (we chose one from the OMM for its wide wavelength range).

3.2 Telluric line removal

As no 'telluric' stars were observed in the OHP campaign, an alternative solution was used to remove the telluric absorption lines. These lines were particularly strong because the star was in a very low position on the sky at the time of the campaign (airmasses of about 2). Nevertheless, SOPHIE's resolving power of 40 000 at 5500 Å (HE mode) can largely resolve these lines, whose width is about 1 Å. So, after removing the non-telluric structures with widths larger than a few angstroms, the lines were fitted with a sum of Gaussians at positions indicated in the IRAF atlas of telluric lines. The results of the fit were then used to divide into each of the spectra to eliminate the telluric contributions.

4 RADIAL VELOCITIES

4.1 O star

The O-star RVs were obtained by measuring the centroid of each relatively narrow photospheric absorption line (allowing for a sloping pseudo-continuum if superposed on WR lines), and by taking the mean of the deduced velocities for each spectrum. We have taken into account a possible shift between the RVs determined from different O-star lines. This was done by choosing one RV set as a reference and by plotting the other sets versus this reference. By fitting a linear curve of slope 1 (i.e. $y = x + b$) into the points, we could then deduce the velocity shift ($= b$) to be subtracted from the considered set. Typical velocity shifts have values from 5 to 10 km s^{-1}. The lines used were: H I 3970.09, 4101.74, 4340.47, 4861.33; He I 4026.19, 4471.48, 5875.62; He II 4199.87, 4541.63, 5411.56 and O III 5590.

4.2 Wolf–Rayet star

The WR-star RVs were estimated by cross-correlation with a reference spectrum, chosen to be unaffected by the wind–wind collision effects. This reference spectrum was constructed by combining all the OHP spectra outside the phase interval 0.98–1.02, where obvious CWR effects occur. The same reference spectrum was used for all the data sets. We used the whole spectral domain of each data source in the correlation and we checked that the excess emission did not critically bias the measurements by testing by eye the shape similarity between the WR and the O RV curves.

4.3 Orbit fit

The measured RVs and errors of the 2009 campaign are presented in Table 2. The typical errors (σ) for each observatory are deduced from the internal dispersion of the differences (RV–fit) between the measurements and the orbital solution (O and WR taken together). The fitted parameters are the period P, the eccentricity e, the time of periastron passage T_0, the longitude of periastron passage in the plane of the orbit measured from the ascending node ω and the semi-amplitudes K(WR) and K(O) of the velocity curves. The RVs were fitted using the IDL[6] routine MPFIT.PRO (Markwardt 2009), which uses the Levenberg–Marquardt technique to solve the least-squares problem. Errors on the parameters are computed by MPFIT using the covariance matrix method applied on the RV errors given in input. We fitted for each set of data an independent γ parameter (= systemic velocity) to best reconnect the different data sets with each other. Observed differences in γ between the sets are of the order of 5–10 km s^{-1} and are most probably instrumental. A weight was attributed to each set based on the external rms dispersion of the measurements minus the model. Data from the previous observational campaigns (M03) were also included in the fit; only the weights were recalculated with our method in order to insure homogeneity. The resulting fit is given in Fig. 1 and the fitted orbit parameters in Table 3.

The differences between the new results and those of M03 are not formally significant at the 3σ level but we have improved the precision on the orbital parameters. We also note that our new period (2896.5 ± 0.7 d instead of 2899.0 ± 1.3 d) agrees better with recent X-ray data repeatability (M. F. Corcoran, private communication). Fits were also made for the WR and the O star separately, which give respectively: $P = 2896.5, e = 0.896, T_0 = 46\,155.8, K(\mathrm{WR}) = -75.7, \omega = 44.5$ and $P = 2896.5, e = 0.897, T_0 = 46\,159.1, K(\mathrm{O}) = 30.6, \omega = 45.2$. This is consistent within the errors with the O/WR simultaneous fit.

5 SPECTRAL CLASSIFICATION

The WR component has been previously confirmed as a WC7pd star, where 'p' refers to its peculiarly broad emission lines (more like WC5) for its WC7 subtype and 'd' refers to its dust-forming events. We see no revision to this classification but we present precise measurements of equivalent widths (EWs) and FWHM of different WR lines (Table 4) and a comparison of these measurements with the classification criteria of Crowther, De Marco & Barlow (1998) (Table 5). However, the spectral type of the O-star component is less clearly identified on our combined mean spectrum, and most

[6] Interactive Data Language, ITT Visual Information Solutions (ITT VIS).

Table 2. RVs of the WR and O components of WR 140. The typical errors (σ) are deduced from the internal dispersion of the differences (RV–fit) between the measurements and the orbital solution (O and WR taken together) for each observatory. RVs are in units of km s^{-1}.

JD – 240 0000	RV(O)	RV–fit	RV(WR)	RV–fit	σ	Obs.
54813.2605	35.1	−4.26	−101.6	−5.08	3.7	OHP
54816.3396	30.3	−10.54	−100.2	−0.12	3.7	OHP
54818.3191	40.5	−1.40	−100.2	2.37	3.7	OHP
54819.3371	37.9	−4.50	−103.3	0.50	3.7	OHP
54820.2146	39.6	−3.22	−107.9	−2.94	3.7	OHP
54821.2162	42.9	−0.46	−109.3	−3.08	3.7	OHP
54822.2497	42.5	−1.37	−112.0	−4.35	3.7	OHP
54823.2120	41.4	−3.03	−112.5	−3.64	3.7	OHP
54828.2995	49.4	2.33	−114.2	1.14	3.7	OHP
54829.2444	51.3	3.79	−117.6	−1.25	3.7	OHP
54834.2488	44.2	−5.01	−126.5	−6.05	3.7	OHP
54835.2263	43.8	−5.53	−123.6	−2.79	3.7	OHP
54836.2219	49.7	0.43	−120.9	−0.10	3.7	OHP
54843.2282	51.1	6.24	−109.6	0.35	3.7	OHP
54844.2272	40.7	−2.75	−105.6	0.77	3.7	OHP
54845.2257	44.0	2.23	−104.4	−2.00	3.7	OHP
54845.2319	42.0	0.20	−106.1	−3.70	3.7	OHP
54846.2475	48.0	8.08	−93.1	4.75	3.7	OHP
54846.2568	47.2	7.28	−92.3	5.53	3.7	OHP
54847.2226	45.3	7.36	−91.4	1.63	3.7	OHP
54852.2358	23.9	−2.76	−66.3	−0.93	3.7	OHP
54853.2322	34.5	10.08	−53.8	5.93	3.7	OHP
54855.2416	24.9	4.90	−49.1	−0.10	3.7	OHP
54857.2429	25.8	9.80	−34.5	4.58	3.7	OHP
54860.2381	13.7	3.01	−19.5	6.80	3.7	OHP
54860.2423	12.7	1.96	−18.7	7.55	3.7	OHP
54861.2456	15.8	6.61	−14.8	7.68	3.7	OHP
54861.2496	13.3	4.17	−16.6	5.87	3.7	OHP
54862.2499	6.7	−1.07	−17.0	2.05	3.7	OHP
54862.2548	5.0	−2.74	−16.5	2.50	3.7	OHP
54873.7413	−3.8	−0.90	7.0	0.01	3.7	OHP
54874.7349	−5.1	−1.63	9.5	1.04	3.7	OHP
54875.7415	−1.5	2.46	9.7	−0.04	3.7	OHP
54877.7303	−7.9	−3.00	12.3	0.22	3.7	OHP
54879.7247	−8.9	−3.17	13.3	−0.83	3.7	OHP
54880.7078	−8.7	−2.55	15.5	0.53	3.7	OHP
54881.7095	−9.4	−2.88	14.2	−1.70	3.7	OHP
54884.7141	−3.7	3.76	17.6	−0.59	3.7	OHP
54885.7229	−11.3	−3.61	20.0	1.19	3.7	OHP
54886.6986	−5.8	2.10	20.3	0.89	3.7	OHP
54888.7010	−8.3	0.12	21.0	0.36	3.7	OHP
54889.7124	−4.6	4.07	18.0	−3.08	3.7	OHP
54890.6953	−15.4	−6.60	19.6	−2.02	3.7	OHP
54893.7053	−9.3	0.10	24.1	1.12	3.7	OHP
54897.6988	−11.9	−1.92	24.9	0.57	3.7	OHP
54897.7015	−8.2	1.72	24.2	−0.22	3.7	OHP
54897.7043	−10.6	−0.63	24.4	0.05	3.7	OHP
54898.7011	−16.5	−6.45	22.9	−1.79	3.7	OHP
54898.7042	−14.3	−4.18	25.4	0.76	3.7	OHP
54898.7073	−16.2	−6.13	24.6	−0.13	3.7	OHP
54900.6852	−14.0	−3.66	21.7	−3.53	3.7	OHP
54900.6883	−13.6	−3.28	22.1	−3.15	3.7	OHP
54900.6914	−18.3	−7.99	20.1	−5.17	3.7	OHP
54901.6822	−8.3	2.15	24.5	−1.02	3.7	OHP
54901.6853	−7.2	3.26	24.5	−0.98	3.7	OHP
54901.6884	−5.0	5.42	26.8	1.29	3.7	OHP
54903.6958	−9.2	1.37	26.5	0.49	3.7	OHP
54905.6836	−12.3	−1.50	23.5	−2.97	3.7	OHP
54906.6655	−3.0	7.88	24.5	−2.14	3.7	OHP
54911.6871	−12.4	−1.20	25.5	−2.04	3.7	OHP

Table 2 – *continued*

JD – 240 0000	RV(O)	RV–fit	RV(WR)	RV–fit	σ	Obs.
54912.6389	−16.1	−4.86	25.6	−2.03	3.7	OHP
54913.6545	−9.4	1.92	28.8	1.03	3.7	OHP
55018.7888	−25.8	−14.04	25.1	−3.67	8.5	OMM
55019.7976	−23.2	−11.44	19.4	−9.33	8.5	OMM
55021.7251	1.8	13.51	32.6	3.92	8.5	OMM
55022.5769	−0.3	11.43	31.0	2.31	8.5	OMM
55023.5802	−12.1	−0.40	26.3	−2.34	8.5	OMM
55026.7784	1.6	13.25	34.1	5.60	8.5	OMM
55028.5613	–	–	27.1	−1.38	8.5	OMM
55033.5434	−19.4	−7.79	17.7	−10.65	8.5	OMM
55035.7731	−10.9	0.60	28.7	0.39	8.5	OMM
55037.7481	−6.0	5.54	32.5	4.28	8.5	OMM
55038.6906	−13.4	−1.85	25.4	−2.85	8.5	OMM
55043.5629	−11.7	−0.28	28.3	0.20	8.5	OMM
55047.5379	−12.7	−1.26	20.3	−7.65	8.5	OMM
55048.5356	–	–	45.0	17.06	8.5	OMM
55049.7346	−34.4	−23.05	16.2	−11.74	8.5	OMM
55050.7467	−6.9	4.45	39.1	11.22	8.5	OMM
55051.7337	−13.0	−1.67	30.1	2.23	8.5	OMM
55052.7340	1.7	13.00	30.2	2.39	8.5	OMM
54578.8834	7.5	−4.06	−26.5	1.79	6.5	DAO
54580.8731	7.6	−4.07	−22.3	6.16	6.5	DAO
54614.7872	19.3	6.40	−36.0	−4.31	6.5	DAO
54615.7836	16.0	3.04	−37.1	−5.31	6.5	DAO
54642.9241	10.7	−3.57	−37.8	−2.94	6.5	DAO
54643.9182	15.6	1.33	−39.2	−4.16	6.5	DAO
54664.7166	25.0	9.59	−36.2	1.58	6.5	DAO
54665.7094	19.0	3.52	−33.3	4.63	6.5	DAO
54675.8039	13.3	−2.79	−34.6	4.86	6.5	DAO
54701.7292	1.0	−16.96	−40.4	3.70	6.5	DAO
54722.7395	9.0	−10.88	−48.4	0.29	6.5	DAO
54723.7921	31.8	11.79	−50.4	−1.51	6.5	DAO
54724.7203	26.7	6.66	−53.9	−4.78	6.5	DAO
54817.3515	39.4	−1.98	−97.0	4.40	7.5	MONS
54818.3541	32.2	−9.68	−106.2	−3.63	7.5	MONS
54819.3206	34.3	−8.03	−108.8	−4.97	7.5	MONS
54820.2973	39.9	−2.96	−115.3	−10.26	7.5	MONS
54821.3117	43.8	0.33	−101.9	4.45	7.5	MONS
54822.3031	40.4	−3.58	−108.7	−1.00	7.5	MONS
54824.3186	44.4	−0.59	–	–	7.5	MONS
54827.3022	41.7	−4.83	−118.0	−3.88	7.5	MONS
54834.3241	40.0	−9.16	–	–	7.5	MONS
54835.3351	40.1	−9.16	−99.9	20.93	7.5	MONS
54836.3579	44.2	−5.09	−117.3	3.50	7.5	MONS
54844.3302	39.0	−4.31	−110.0	−3.95	7.5	MONS
54846.3243	44.6	4.82	−85.3	12.16	7.5	MONS
54852.3204	24.8	−1.64	−71.8	−6.98	7.5	MONS
54853.3189	19.2	−5.02	−67.5	−8.24	7.5	MONS
54855.3129	23.4	3.59	−59.4	−10.81	7.5	MONS
54856.3128	25.2	7.38	−48.0	−4.41	7.5	MONS
54858.7387	8.4	−4.83	−28.9	3.54	7.5	MONS
54859.7453	18.9	7.33	−19.5	8.74	7.5	MONS
54860.7312	18.4	8.42	−30.2	−5.75	7.5	MONS
54861.7234	34.0	25.50	–	–	7.5	MONS
54865.7312	8.0	4.50	0.9	9.54	7.5	MONS
54871.7333	−2.6	−0.96	−13.5	−17.38	7.5	MONS
54873.7436	−4.8	−1.93	7.0	−0.01	7.5	MONS
54874.7614	0.3	3.80	3.5	−4.97	7.5	MONS
54876.7646	2.0	6.50	−4.4	−15.39	7.5	MONS
54878.7469	−12.7	−7.37	9.5	−3.66	7.5	MONS
54887.6717	1.4	9.53	28.1	8.06	7.5	MONS
54890.6937	−5.7	3.16	20.1	−1.52	7.5	MONS
54891.6738	−6.9	2.12	29.5	7.42	7.5	MONS
54892.6705	−9.1	0.11	32.9	10.40	7.5	MONS

Table 2 – *continued*

JD – 240 0000	RV(O)	RV–fit	RV(WR)	RV–fit	σ	Obs.
54900.6975	−14.4	−4.08	–	–	7.5	MONS
54907.6390	−11.3	−0.31	30.0	3.22	7.5	MONS
54912.6621	−12.9	−1.58	38.1	10.47	7.5	MONS
54838.2352	40.4	−8.55	−100.8	19.12	11.0	BS
54840.2001	48.0	0.13	−111.0	6.40	11.0	BS
54841.2043	41.7	−5.38	−101.2	14.25	11.0	BS
54842.2012	49.7	3.58	−105.9	7.11	11.0	BS
54843.2125	45.7	0.83	−95.4	14.58	11.0	BS
54845.2213	32.6	−9.20	−102.9	−0.45	11.0	BS
54852.2053	22.7	−4.08	−81.3	−15.77	11.0	BS
54857.2025	27.0	11.02	−66.7	−27.40	11.0	BS
54861.2139	20.9	11.66	–	–	11.0	BS
54861.2140	–	–	−40.5	−17.85	11.0	BS
54445.2470	–	–	−29.6	−10.11	9.0	THO
54446.2376	–	–	10.9	30.46	9.0	THO
54464.3585	−8.3	−16.70	−9.9	10.60	9.0	THO
54472.2292	–	–	−32.7	−11.77	9.0	THO
54482.2175	−8.9	−17.72	−16.0	5.54	9.0	THO
54495.6969	3.5	−5.63	−17.3	5.02	9.0	THO
54572.5640	4.9	−6.41	−43.9	−16.12	9.0	THO
54600.4890	0.8	−11.55	−31.1	−0.84	9.0	THO
54748.3681	19.5	−3.34	−58.5	−2.53	9.0	THO
54795.2708	24.7	−7.74	−80.3	−0.69	9.0	THO
54800.2354	29.8	−4.36	−84.3	−0.69	9.0	THO
54802.3446	38.7	3.84	−83.6	1.81	9.0	THO
54803.2519	31.6	−3.57	−85.0	1.20	9.0	THO
54810.2058	28.5	−9.54	−97.1	−4.02	9.0	THO
54811.2458	42.8	4.32	−118.7	−24.48	9.0	THO
54826.2450	55.2	9.14	−115.3	−2.51	9.0	THO
54827.2396	45.9	−0.59	−111.6	2.44	9.0	THO
54828.2719	47.3	0.28	−106.6	8.68	9.0	THO
54829.2202	–	–	−107.0	9.33	9.0	THO
54830.2334	52.2	4.25	−113.6	3.80	9.0	THO
54831.2206	–	–	−119.3	−0.94	9.0	THO
54833.2167	57.3	8.38	−112.2	7.72	9.0	THO
54837.2858	–	–	−123.2	−2.69	9.0	THO
54844.2330	39.6	−3.81	−106.9	−0.52	9.0	THO
54845.2511	43.5	1.74	−107.3	−4.95	9.0	THO
54851.2443	32.3	3.36	−81.6	−10.63	9.0	THO
54854.2303	24.7	2.56	−62.3	−8.04	9.0	THO
54855.2592	34.3	14.35	−52.8	−3.91	9.0	THO
54856.2249	26.6	8.67	−45.1	−1.16	9.0	THO
54857.2431	28.7	12.75	−39.0	0.06	9.0	THO
54866.6723	–	–	−3.3	3.00	9.0	THO
54870.2430	−0.8	−0.31	7.0	5.71	9.0	THO
54874.2506	0.3	3.48	13.6	5.82	9.0	THO
54882.6374	–	–	14.7	−1.93	9.0	THO
54892.6583	1.9	11.12	25.6	3.13	9.0	THO
54895.5894	−6.6	3.02	27.8	4.18	9.0	THO

especially its luminosity class. The determination of this luminosity class is of prime importance for the determination of the distance and to deduce information about the O-star wind. The quality of the OHP spectra provides an opportunity to extract this luminosity class.

Given the dominating strength of the WR spectrum, it is useful to apply a spectral decomposition technique to isolate the O-star spectrum. We therefore used the shift-and-add technique of Demers et al. (2002), with our new orbital solution. In this procedure, we first co-add all the spectra in the WR frame of reference, by correcting each spectrum from its orbital velocity (taken on the fitted curve and not the individual measurements). This 'dilutes' the O-star absorption lines and leads to a first estimation of the WR spectrum. We then subtract this spectrum from all the original spectra and co-add the differences this time in the O-star frame of reference, which leads to an estimation of the O spectrum. This spectrum is subtracted from the original spectra and the differences are co-added again in the WR frame of reference, and so on, until the co-added spectrum for each star converges, which generally happens in fewer than 10 iterations. The result of the spectral separation is shown in Fig. 2. The whole OHP data set was used. As noted above, no revision is required for the WR-star spectral class. Concerning the determination of the O-star spectral class, the main criterion is the EW ratio of He I λ4471 to He II λ4541 (W') (Conti & Alschuler 1971). We measure $\log(W') \simeq -0.37 \pm 0.09$, which implies the O star is O5.5–O6, with a preference for O5.5, which is consistent with the observed absence of Si IV λ4089.

The luminosity class determination is limited by the deteriorated information in the He II 4686 Å region. Indeed, this region is dominated by the residuals of the variability effects of the C III/IV+He II emission blend of the WR star. We cannot really distinguish between absorption and emission for this line, although we do note that there is no narrow residual component, either emission or absorption, as expected from the O star. Using the strength of the N III and C III emissions lines (which are narrow, as required if arising in the O star) in the vicinity of 4645 Å and based on the criteria in Walborn et al. (2010), we deduce a type of O5.5fc for the O star, with a luminosity class somewhere between III and I (there is no II defined).

We now examine the line dilution of the O star by the WR-star light. With conservation of line flux,

$$\text{line flux} = I_c(\text{O} + \text{WR}) \times ew_{\text{obs}} = I_c(\text{O}) \times ew_{\text{exp}}, \quad (1)$$

where ew_{obs} and ew_{exp} are the observed and expected EWs, respectively, for a single O star of the same spectral type, and I_c is the continuum intensity. We can then write

$$\frac{I_c(\text{O})}{I_c(\text{O} + \text{WR})} = \frac{ew_{\text{obs}}}{ew_{\text{exp}}} \quad (2)$$

and

$$\frac{10^{-0.4M_V(\text{WR})} + 10^{-0.4M_V(\text{O})}}{10^{-0.4M_V(\text{O})}} = 1 + 10^{-0.4[M_V(\text{WR}) - M_V(\text{O})]}. \quad (3)$$

Here, M_V designates the absolute visual magnitude in the V band. We finally obtain the following estimation formula:

$$M_V(\text{WR}) - M_V(\text{O}) = -2.5 \log \left(\frac{ew_{\text{exp}}}{ew_{\text{obs}}} - 1 \right). \quad (4)$$

We measured the line EWs of the disentangled O-star spectrum and of two template stars successively: HD 97253, a typical single O5.5 III star, and HD 163758, an O6.5f Ia with the suggestion of a C overabundance, which makes it quite close to our O-star spectral-type estimation. These spectra were both found in the UVES POP data base (Bagnulo et al. 2003). No O5.5/O6 I star was available. These measurements are shown in Table 6. We choose to apply equation (4) to the hydrogen lines only in order to minimize the effects of differences in helium content between the two stars. By averaging over the hydrogen lines, we obtain an EW ratio $ew_{\text{obs}}/ew_{\text{exp}} = 0.43 \pm 0.04$, which yields a difference in magnitude of -0.3 ± 0.2 (WR slightly brighter than the O star) with the O5.5 III template star. When making the same calculation on the He II lines, we obtain an average ratio of 0.59 ± 0.03 and a difference in magnitude of 0.4 ± 0.1 (O star brighter).

If we take a typical O5.5 III absolute magnitude of $M_v = -4.9$ from Martins, Schaerer & Hillier (2005), we obtain for the WR star

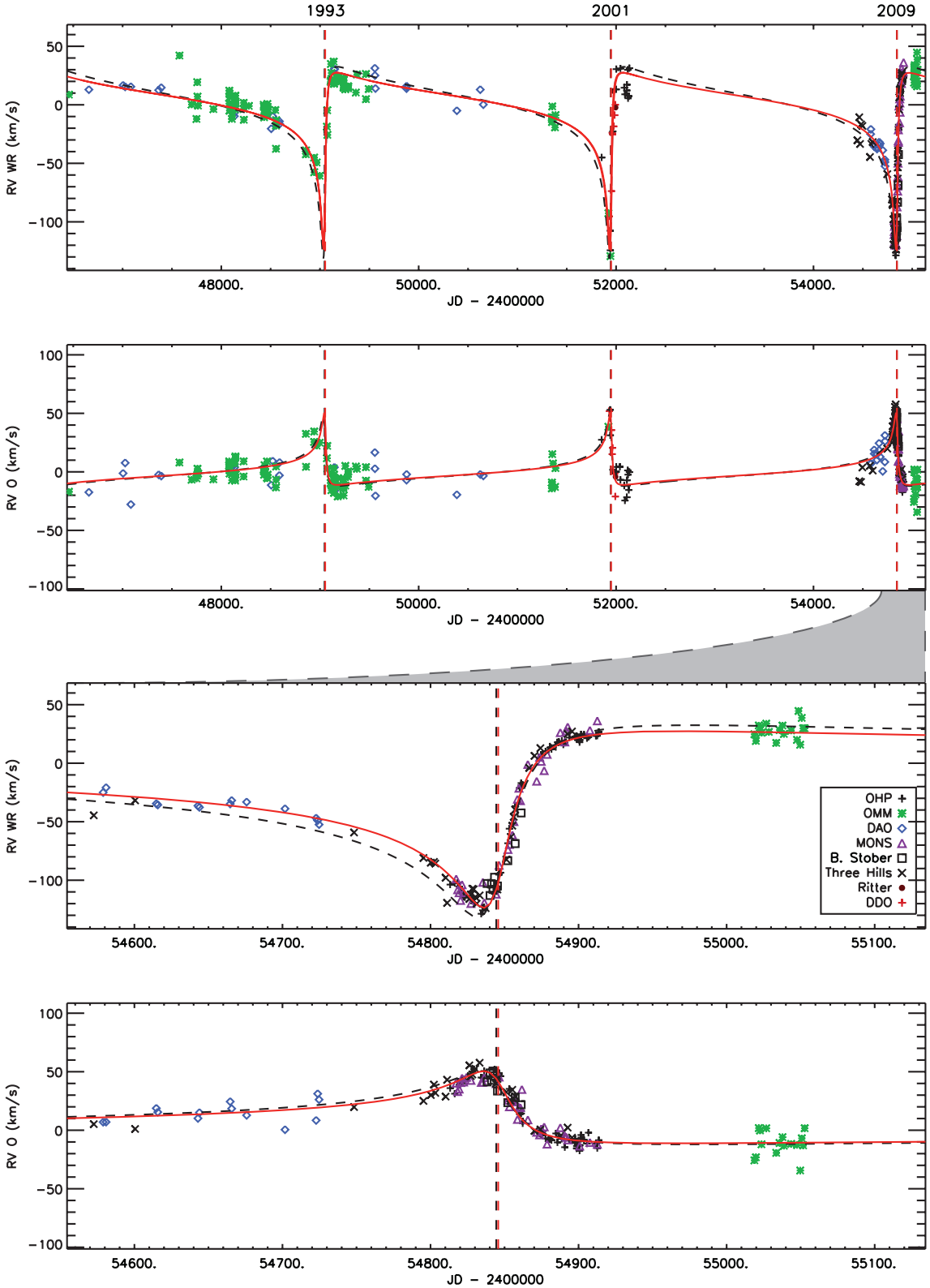

Figure 1. Top two panels: measured RVs of the WR star and of the O star, together with the fit for the orbital solution (full line) whose best-fitting parameters are given in Table 3. We have included data from the last periastron campaign in 2001 (M03) taken at David Dunlap Observatory (DDO), OHP, Ritter Observatory, DAO and OMM. The black dashed line is the orbital solution from M03. The dashed vertical lines show the position of the new periastron passage. Both 'old' and 'new' periastron passages are shown. Bottom two panels: same plots but zoomed on the 2009 campaign (the grey-filled curve between panels two and three illustrates the X-axis expansion).

Table 3. New orbit parameters for WR 140 compared with the values from M03.

Parameter	This paper + M03	This paper	M03
K(WR) (km s^{-1})	-75.5 ± 0.7	-75.3 ± 0.9	-82.0 ± 2.3
K(O) (km s^{-1})	30.9 ± 0.6	30.7 ± 0.6	30.5 ± 1.9
$a \sin(i)$(WR) (au)	8.92 ± 0.15	8.98 ± 0.17	10.29 ± 0.47
$a \sin(i)$(O) (au)	3.646 ± 0.085	3.665 ± 0.093	3.81 ± 0.27
P (d)	2896.5 ± 0.7	2896.5	2899.0 ± 1.3
e	0.8962 ± 0.0014	0.894 ± 0.002	0.881 ± 0.005
T_0 (HJD 240 0000+)	46156.2 ± 2.2	46157.0 ± 0.5	46147.4 ± 3.7
ω (deg)	44.6 ± 1.1	47.5 ± 1.7	46.7 ± 1.6

Table 4. EWs and FWHM measured on different WR emission lines. The typical FWHM of C III/IV+He II for a regular WC7 star would be 31 ± 5 Å (Torres et al. 1986); we measure 67 ± 2, which is closer to WC5 typical values (i.e. 64 ± 15 Å). This justifies the 'peculiar' denomination in the classification.

Line or blend	$\log(ew_\lambda)$	FWHM (Å)
C III/IV+He II 4650, 4658, 4686	2.348 ± 0.005	67 ± 2
O III–V 5590	1.05 ± 0.04	75 ± 2
C III 5696	1.87 ± 0.01	94 ± 2
C IV+He I 5808, 5876	2.413 ± 0.004	71 ± 2
C IV 5808	2.215 ± 0.006	51 ± 2

an absolute visual magnitude of -5.2 ± 0.2 with the H lines and -4.5 ± 0.1 with the He II lines, which is consistent with a typical WC7 star magnitude of around -4.8 (Smith, Shara & Moffat 1990).

We now use the O6.5 Ia template. We obtain a difference in magnitude of 0.7 ± 0.4 with the H lines only, and roughly the same with the He II lines. Given a typical O5.5 I magnitude of $M_V = -6.3$ (Martins et al. 2005), this yields $M_V = -5.6 \pm 0.4$ for the WR, which is also consistent with WC7 typical magnitudes.

We computed the corresponding photometric distances using the extinction model of Amôres & Lépine (2005) in order to compare these with the value of Dougherty et al. (2005, hereafter D05) (i.e. 1.85 ± 0.16 kpc). For the class III template, we obtain $d = 2.1 \pm 0.1$kpc when using the H lines and $d = 1.9 \pm 0.1$kpc with the He II lines. For the class Ia template, we have $d = 2.6 \pm 0.1$kpc. This would suggest a class III in order to be consistent with D05. However, given the multiple sources of uncertainties of this method, we cannot exclude a class I star with certitude.

It is also interesting to make the opposite reasoning and to try to evaluate the line dilution of the WR star by the O-star light. Based on the work of Torres, Conti & Massey (1986) (their fig. 2) and Smith et al. (1990) (their table 5), and given the fact that WR 140 shows broader lines than standard WC7 stars (values more typical of WC5 stars; Torres et al. 1986), we chose an expected value of $\log(ew_{\rm exp}) \simeq 3.0$ for 4650 and 5880 (a typical value for a 'regular' WC7 star would be more likely to be 2.2–2.5). The errors on these empirical values are about 0.3. Our measured values are $\log[ew(4650)] \simeq 2.34$ and $\log[ew(5808)] \simeq 2.21$, which lead to two estimations for the difference in magnitude between the stars: 1.4 and 1.1, respectively. This makes the O star about three times brighter than the WR in the optical band. If we assume a reasonable absolute V magnitude of -4.8 for the WR star (Smith et al. 1990), we have for the O star $M_V = -5.9$ to -6.2, which is compatible with both class I and III magnitudes (Martins et al. 2005).

As a conclusion, we are not able here to distinguish between class I and III for the O5.5/6 star. Note, however, that this task is complicated by the fact that the magnitude gap between these classes is very small for this particular spectral type (O5–6).

6 EXCESS EMISSION

6.1 Lührs model fit

The shock cone around the O star produces excess emission that can be easily observed on the C III 5696 and He I 5876 flat top lines. This excess emission first appears just before periastron passage, on the blue side of the line, and then moves quickly to the red side just after periastron passage, before it disappears shortly thereafter. We measured this excess in the OHP data by subtracting a reference spectrum from each spectrum of the set. This reference spectrum has been constructed by co-adding the OHP spectra outside phases 0.98–1.02, unaffected by wind–wind collision effects. We took care, before doing the subtraction, to remove the O-star spectral signatures, notably the narrow emission feature on top of the C III 5696 line, by fitting a Gaussian and subtracting it from each profile. The result of this procedure is shown in Fig. 3.

We can analyse the excess emission by using a simple geometric model of the CWR developed by Lührs (1997). The model takes into account the half-opening angle of the shock cone θ, the velocity of the plasma along the cone $v_{\rm strm}$ and the orbital inclination i. The CWR is assumed to be curved in the plane of the orbit and its orientation over a limited range of the shock cone is parametrized by a single angle, $\delta\phi_0$, for simplicity (see Fig. 4). By a simple integration of the emissivity on a thick slice of the cone where the emission is supposed to arise, the model provides theoretical excess profiles showing double peaks moving with the orbit. However, depending on the spectral resolution and the velocities and geometry of the shock cone, the double peaks might not be visible. Faced with this situation, we can still derive some valuable estimates of the colliding-wind region by measuring the entire excess emission. Hill et al. (2000) and Hill, Moffat & St-Louis (2002) have shown that, for a circular orbit, the width (e.g. FWHM) and position of the excess emission vary as

$$FW_{\rm ex} = C_1 + 2v_{\rm strm} \sin\theta \sqrt{1 - \sin^2 i \cos^2(\phi - \delta\phi_0)} \quad (5)$$

Table 5. Comparison between measurements and classification criteria from Crowther et al. (1998) for the WR component.

Criterion	Measurement	WC7 value	WC5 value
FWHM C IV 5808 (Å)	51 ± 2	45 ± 20	50 ± 20
FWHM C IV+He I 5808, 5876	71 ± 2		
C IV 5808/C III 5696 [log(ew)]	0.35 ± 0.01	$+0.1$ to $+0.6$	-1.1 to $+1.5$
C IV+He I 5808, 5876/C III 5696	0.543 ± 0.007		
C III 5696/O III–V 5590	0.82 ± 0.04	≥ 0.1	-0.4 to 0.5

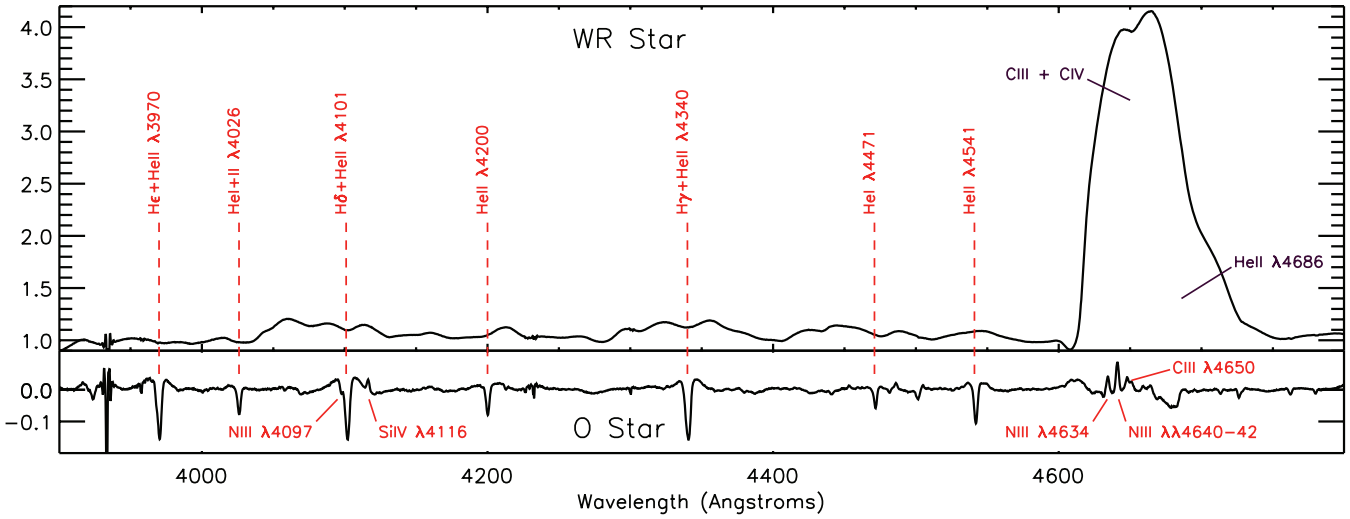

Figure 2. Result from the 'shift-and-add' method for spectrum decomposition. The Y scale for the O star has been expanded by a factor of 3. Note that this technique does not yield absolute line strengths.

Table 6. Measured EWs for the O-star component of WR 140 compared with those for the O5.5 III star, HD 97253, and the O6.5 Ia star, HD 163758.

Line	WR 140	HD 97253	Ratio	HD 163758	Ratio
Hε+He II λ3970	0.67 ± 0.01	1.54 ± 0.02	0.435 ± 0.009	0.98 ± 0.02	0.68 ± 0.02
He I+II λ4026	0.24 ± 0.01	0.40 ± 0.01	0.60 ± 0.03	0.60 ± 0.01	0.40 ± 0.02
Hδ+He II λ4101	0.78 ± 0.01	1.83 ± 0.02	0.426 ± 0.007	1.42 ± 0.02	0.55 ± 0.02
He II λ4200	0.296 ± 0.005	0.48 ± 0.01	0.62 ± 0.02	0.43 ± 0.01	0.68 ± 0.02
Hγ+He II λ4340	0.778 ± 0.005	2.02 ± 0.01	0.385 ± 0.003	1.22 ± 0.01	0.637 ± 0.007
He I λ4471	0.187 ± 0.005	0.25 ± 0.01	0.75 ± 0.04	0.59 ± 0.01	0.32 ± 0.01
He II λ4541	0.395 ± 0.005	0.65 ± 0.01	0.61 ± 0.01	0.68 ± 0.01	0.58 ± 0.01
Hβ+He II λ4861	0.891 ± 0.005	1.82 ± 0.01	0.490 ± 0.004	1.15 ± 0.01	0.775 ± 0.008
He II λ5412	0.536 ± 0.005	0.97 ± 0.02	0.55 ± 0.01	0.80 ± 0.02	0.67 ± 0.02
O V λ5590	0.177 ± 0.005	0.18 ± 0.02	1.0 ± 0.1	0.30 ± 0.02	0.59 ± 0.04

and

$$RV_{\rm ex} = C_2 + v_{\rm strm}\cos\theta\sin i\cos(\phi - \delta\phi_0). \quad (6)$$

Here, C_1 and C_2 are simple constants and ϕ is the orbital azimuthal angle (or true anomaly for $\omega = 270^\circ$) in the case of a circular orbit $\phi = 360^\circ \times$ phase and the WR star is in front at $\phi = 0$.

Unlike the cases for WR 42, WR 48 and WR 79, described by Hill et al. (2000; 2002), we face additional complications here. The orbit is not circular and we do not have full phase coverage. To circumvent the first complication, we can still fit versus true anomaly (calculated from the known orbit), and proceed as if the orbit was circular. We also need to replace ϕ by $\phi - [90^\circ - \omega]$ in equations (5) and (6), where ϕ is now the true anomaly for an eccentric orbit; $\phi = 0$ is the periastron passage and $\phi = 90^\circ - \omega$ has the WR in front. The lack of phase coverage is not as bad as it appears at first sight, as the very limited phase interval over which excess emission is measurable actually corresponds to about 150° of true anomaly. Using this model to fit the data, we obtain $v_{\rm strm} = 2090 \pm 90$ km s^{-1}, $i = 53 \pm 6^\circ$, $\theta = 42 \pm 3^\circ$ and $\delta\phi_0 = 21 \pm 3^\circ$ (see plot in Fig. 5). However, we can go a bit further in modifying the Lührs model for an eccentric orbit by allowing the parameter $\delta\phi_0$ (now denoted $\delta\phi$) to vary throughout the orbital motion.

Two different effects will affect $\delta\phi$. The first is the aberration effect (or Coriolis effect), which will produce an angular shift (Moffat et al. 1998):

$$\delta\phi = \arctan\left[\frac{v_\theta}{v_{\rm wind}({\rm WR}) + v_{\rm wind}({\rm O})}\right].$$

Here, v_θ is the azimuthal component of the orbital velocity of the O star in the WR frame of reference (or inversely). This velocity is deduced from the angular momentum conservation:

$$r v_\theta = J = \sqrt{G(M_{\rm WR} + M_{\rm O})a(1 - e^2)}$$

and

$$r = \frac{a(1 - e^2)}{1 + e\cos\phi}.$$

However, in our case, this effect will only contribute to a maximum angular shift of 2.6° at periastron, and will fall quickly to 0 subsequently. This is far from the 22° needed to fit the data.

The second factor contributing to $\delta\phi$ is the curvature of the shock surface. If we assume that after being shocked at time t, the wind plasma moves in a rectilinear motion with a velocity $v_{\rm strm}$ along the 'local' Lührs cone, and that the distance from the apex to the excess-forming region (EFR) is constant throughout the orbit, it will take a time δt (or a phase fraction $\delta p = \delta t/P$) for this plasma to reach the EFR. The 'local' Lührs cone emitting the excess at phase p will therefore appear shifted by an angle

$$\delta\phi = \phi(p) - \phi(p - \delta p).$$

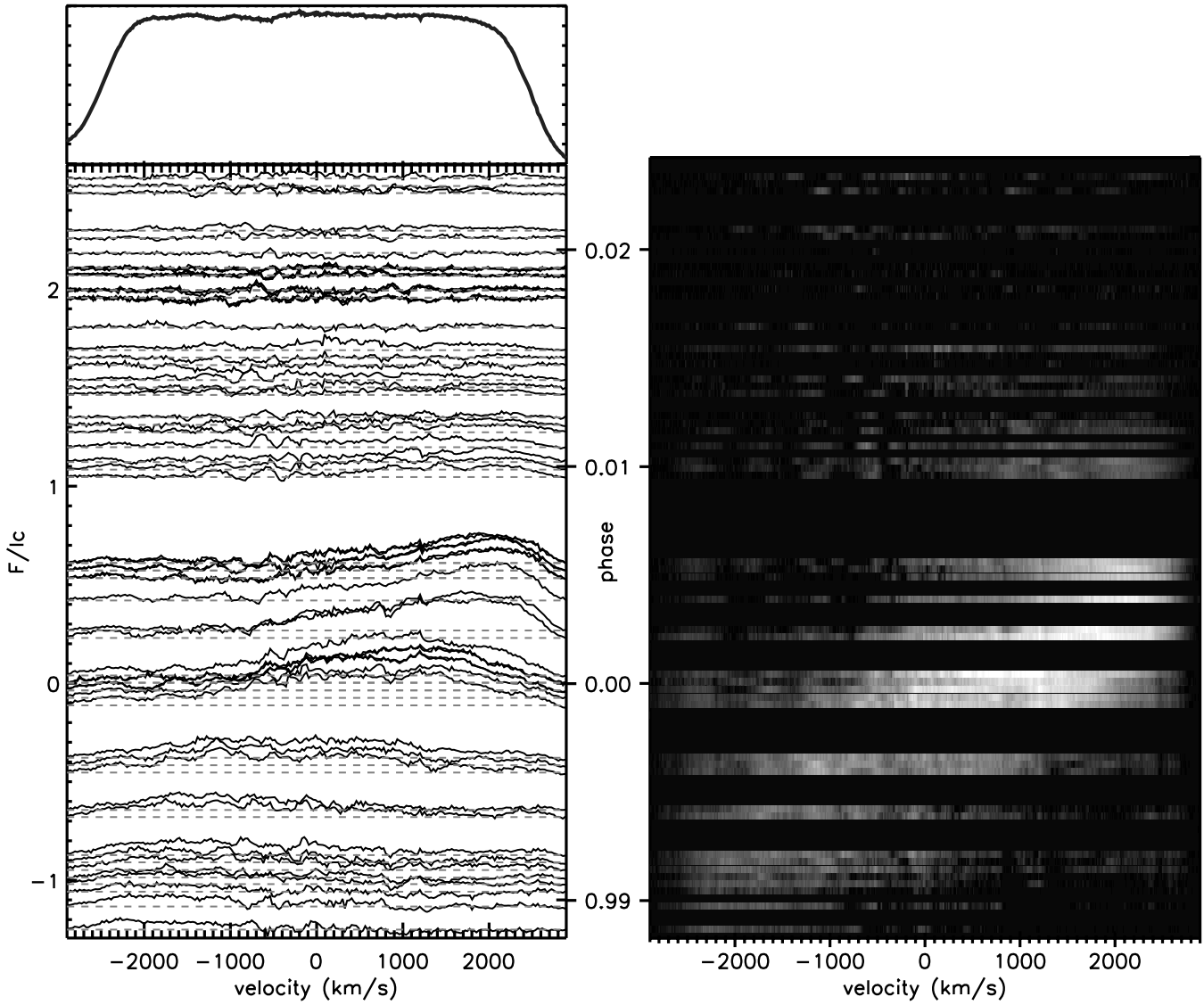

Figure 3. Left: the C III 5696 flat top line excess emission as a function of the orbital phase for the OHP data only. This has been obtained by subtracting a reference profile (top panel) from all the spectra. Right: same as left but plotted in grey-scale.

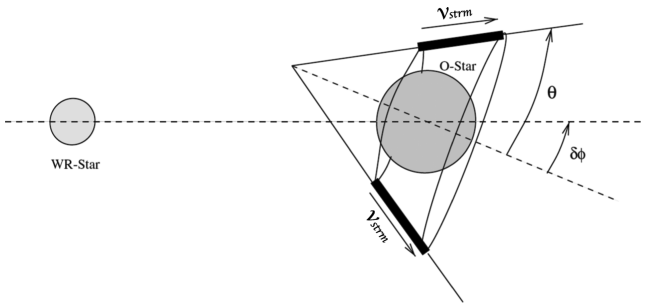

Figure 4. Schematic view of the geometric model by Lührs (1997) taken from Bartzakos, Moffat & Niemela (2001) (their fig. 2).

We can then use the parameter δp (i.e. a constant phase shift) to fit instead of $\delta\phi$ (a shift in true anomaly), which has the advantage of being consistent with the orbit. Using equations (5) and (6) and the modifications described above (Coriolis + phase shift δp), we have fitted the measurements of the width and position of the excess emission shown in Fig. 5. The evolution of $\delta\phi$ with phase is shown in Fig. 6.

The position of the excess was computed with the first moment formula

$$RV = \frac{c(\bar{\lambda} - \lambda_0)}{\lambda_0} \quad \text{with} \quad \bar{\lambda} = \int_{\lambda_1}^{\lambda_2} F(\lambda)\lambda \, \mathrm{d}\lambda \Big/ \int_{\lambda_1}^{\lambda_2} F(\lambda) \, \mathrm{d}\lambda, \quad (7)$$

where λ_0 is the central wavelength of the line and λ_1 and λ_2 are the limits of the excess profile.

Instead of the FWHM, which is too sensitive to the irregularities of the profiles, the width was computed as the second central moment of the excess

$$FW = \frac{2.35c}{\lambda_0} \left[\int_{\lambda_1}^{\lambda_2} F(\lambda)(\lambda - \bar{\lambda})^2 \, \mathrm{d}\lambda \Big/ \int_{\lambda_1}^{\lambda_2} F(\lambda) \, \mathrm{d}\lambda \right]^{1/2}, \quad (8)$$

where 2.35 is the factor linking the FWHM and σ for a Gaussian profile (FWHM $= 2.35 \times \sigma$). Of course, our profiles are not strictly Gaussians but they are not extremely different either. The errors were obtained by applying the error propagation formulae to

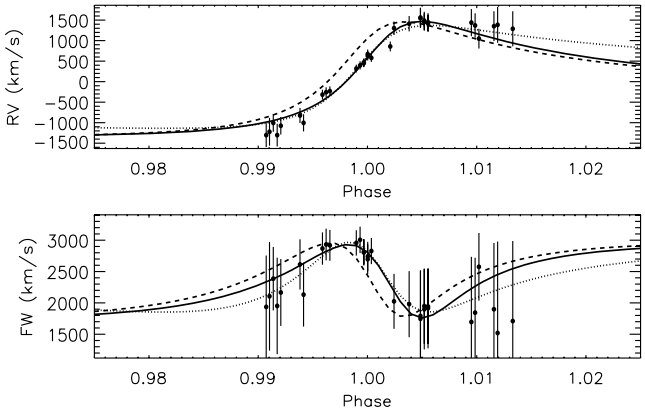

Figure 5. Fit of the RV and width of the excess using the original (dotted line) and the modified (full line) Lührs model. The dashed line shows the solution from M03. The resulting parameters of the fit are listed in Table 8. The measured RVs and FWs are presented in Table 7.

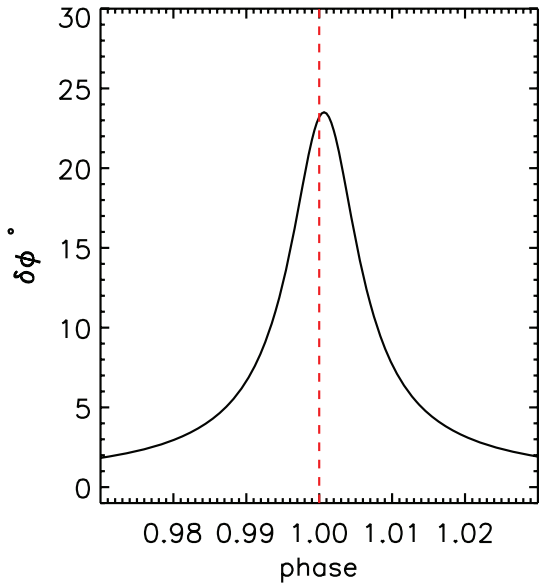

Figure 6. The angle $\delta\phi$ as a function of phase resulting from the combined action of the Coriolis effect (nearly negligible) and a constant phase shift of 0.0014 (or 4.0 d) corresponding to the flow time from the apex to the EFR.

equations (7) and (8) and taking into account the Poisson noise and readout noise of $F(\lambda)$. The measured RVs and FWs are presented in Table 7.

Reasonable fits are obtained for a very wide range of parameters, but some limits can be derived by making a few realistic assumptions. For example, we can require that the velocity of the gas streaming along the bow shock cone, $v_{\rm strm}$, does not exceed the terminal velocity of the WR wind, v_∞. Eenens & Williams (1994) find $v_\infty = 2900$km s^{-1} for the WR-star component of WR 140. Another possible constraint can be obtained by assuming that turbulence in the shock cone contributes to the constant C_1 in equation (5). Hill et al. (2002) found that numbers of the order of 200–500 km s^{-1} were appropriate for WR 42, WR 48 and WR 79 in this respect.

We finally find $v_{\rm strm} = 2170 \pm 100$ km s^{-1}, $i = 55 \pm 6^\circ$, $\theta = 39 \pm 3^\circ$ and $\delta p = 0.0014 \pm 0.0002$ corresponding to $\delta\phi$ at periastron $= 23^\circ$ (versus $v_{\rm strm} = 2300 \pm 500$ km s^{-1}, $i = 50 \pm 15^\circ$, $\theta = 40 \pm 15^\circ$ and $\delta\phi_0 = 40 \pm 20^\circ$ from M03). Our value of i is compatible with that from D05, $i = 122 \pm 5^\circ$, equivalent to $180 - i = 58^\circ$, given the fact that we cannot distinguish between i and $180 - i$ with the Lührs fit alone. The errors on the parameters are those computed by MPFIT, using the errors on $F(\lambda)$ given in input (typically around 0.006 in continuum units). Applying the approach of Cantó, Raga & Wilkin (1996) (their equation 28), we find that our value of θ leads to $\eta = [\dot{M}(\mathrm{O})v_\infty(\mathrm{O})]/[\dot{M}(\mathrm{WR})v_\infty(\mathrm{WR})] = 0.039 \pm 0.016$ (versus 0.045 from M03 and 0.02 from Pittard & Dougherty 2006). The difference between the estimations of η are discussed in Section 6.2. Our value for the inclination finally gives the following estimation for the stellar masses: $M_{\rm WR} = 16 \pm 3$ M$_\odot$ and $M_{\rm O} = 41 \pm 6$ M$_\odot$ (versus 19 and 50 M$_\odot$ from M03). The O-star mass agrees well with O5.5 stars between luminosity classes III and I given by Martins et al. (2005) (as deduced in Section 5). The WR mass can be compared with measurements of other WC-type stars of the 'VIIth catalogue of galactic Wolf–Rayet stars' (van der Hucht 2001). This latter gives for WC6–8-type stars, masses between 9.5 M$_\odot$ (γ Vel) and 16 M$_\odot$ (HD 94305). A list of all the parameters deduced in this study is presented Table 8.

The same analysis carried out for the He I 5876 line shows qualitatively the same behaviour of the excess emission. However, the RV and FWHM measurements are of lesser quality and no additional information was deduced. The inferior quality is mainly because of the blending of He I with the C IV 5806 emission feature (also

Table 7. Measured RVs, full widths and EWs of the C III 5696 excess emission for the OHP data. Units are km s^{-1}.

JD – 240 0000	RV	σ	FW	σ	EW	σ
54819.3371	−1302	292	1935	819	2.38	0.34
54820.2146	−1221	338	2105	866	1.65	0.28
54821.2162	−1005	214	2386	506	3.30	0.40
54822.2497	−1303	276	1951	770	2.67	0.36
54823.2120	−1074	213	2166	533	3.46	0.41
54828.2995	−823	183	2613	400	3.84	0.43
54829.2444	−1003	209	2131	509	3.24	0.40
54834.2488	−316	120	2867	257	5.81	0.53
54835.2263	−256	119	2931	253	5.92	0.54
54836.2219	−230	115	2917	246	6.14	0.55
54843.2282	318	95	2956	202	9.78	0.69
54844.2272	395	100	3005	210	9.63	0.69
54845.2257	468	97	2804	207	9.82	0.70
54845.2319	450	95	2815	203	10.06	0.70
54846.2475	671	112	2697	237	8.84	0.66
54846.2568	626	110	2740	233	8.77	0.66
54847.2226	579	98	2827	208	10.95	0.74
54852.2358	858	121	2936	253	10.34	0.71
54853.2322	1303	161	2024	438	7.89	0.62
54857.2429	1411	187	1979	526	6.70	0.57
54860.2381	1561	240	1747	769	4.67	0.48
54860.2423	1545	231	1790	722	5.01	0.50
54861.2456	1451	210	1948	600	5.54	0.52
54861.2496	1484	218	1898	640	5.28	0.51
54862.2499	1448	220	1915	640	5.01	0.50
54862.2548	1421	208	1942	596	5.44	0.52
54873.7413	1438	330	1695	1039	2.12	0.32
54874.7349	1369	296	1844	875	2.47	0.35
54875.7415	1048	241	2575	539	2.92	0.38
54877.7303	448	204	3261	407	2.77	0.37
54879.7247	1351	364	1898	1057	1.62	0.28
54880.7078	1385	437	1520	1457	1.11	0.23
54884.7141	1288	427	1710	1276	1.05	0.22
54890.6953	202	197	3165	411	2.42	0.34

Table 8. New parameters for WR 140, deduced from the modified Lührs model, compared with the values from M03.

Parameter	This paper	M03
i (deg)	55 ± 6	50 ± 15
C_1	200	$200 - 500$
C_2	71 ± 55	$100 - 200$
$v_{\rm strm}$ (km s^{-1})	2170 ± 100	2300 ± 500
θ (deg)	39 ± 3	40 ± 15
$\delta\phi$ (deg)	23 (at phase = 0)	40 ± 20
δp	0.0014 ± 0.0002	
a(WR) (au)	10.9 ± 0.8	13.5 ± 3.0
a(O) (au)	4.4 ± 0.3	5.0 ± 1.1
M(WR) ($M_\odot$)	16 ± 3	19
M(O) ($M_\odot$)	41 ± 6	50
η	0.039 ± 0.016	0.045 ± 0.075

restricting the placement of the continuum), along with residuals from imperfect removal of telluric lines and the blaze correction.

An important remark is that whereas the measurement of the position of the excess is quite robust (even for the He I 5876 line), its width is very dependent on the details of the measurement (boundaries in the moment integral, minimum flux for pixel selection in the integral, etc.). The errors on the width have been artificially increased in order to reflect this source of uncertainty. We should also note several caveats when deducing the wind momentum ratio from half-opening angles. First, the opening angles of the O-star and WR-star shocks are in general different, and different from that of the contact discontinuity (only in highly radiative systems where the interaction region is very thin are all three identical). Usually, it is assumed that the measured half-opening angle is that of the contact discontinuity, and the wind momentum ratio is then derived using, for example, the equation in Cantó et al. (1996). However, it is not so obvious that this is correct. We know, for instance, that in an adiabatic system, the total emission is dominated by the stronger wind (Stevens, Blondin & Pollock 1992). In our case, the CWR is suspected to be radiative at the time where the excess emission arises, as the $1/r^2$ law in Fig. 7 suggests. However, it would certainly turn adiabatic later in the orbit as the two stars become more distant. These details need further investigation.

6.2 Discussion

We can see that our estimation of the wind momentum ratio η is consistent with the estimation of M03. Our value is also in line with the estimation by Pittard & Dougherty (2006) (i.e. $\eta = 0.02$) based on radio-emission modelling. They computed mass-loss rates required to match the observed X-ray flux at 3 keV as a function of η (their table 2). According to this study, our value of η gives $\dot{M}$(WR) $\simeq 3 \times 10^{-5}$ and $\dot{M}$(O) $\simeq 1 \times 10^{-6}$M$_\odot$yr^{-1}. The terminal velocities assumed in the calculations are v_∞(WR) = 2860 km s^{-1} (D05) and v_∞(O) = 3100km s^{-1} (Setia Gunawan et al. 2001). We can argue that the comparison between the two determinations of η are biased by the fact that we are looking at diagnostics from two very different regions of the shock: very close to the apex for the radio emission, where the shocks are strongest (and hence most efficient in accelerating particles), and much further away for the optical excess emission. The similarity between our value and that of Pittard & Dougherty (2006) would therefore imply that the opening angle is constant along the cone. Again, note that these opening angles refer to the 'local' Lührs cones defined by the orientation of the flow velocities at a radius $r(t)$ from the apex.

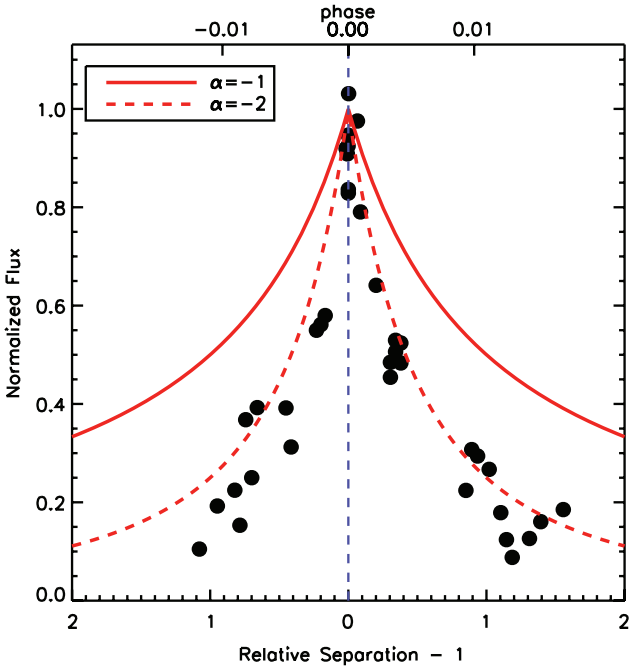

Figure 7. Normalized flux of the excess as a function of the relative separation of the two stars $[(d - d_{\rm min})/d_{\rm min}]$. The full line shows a d^{-1} dependency, expected for an adiabatic emission process. The dashed line shows a d^{-2} dependency, possibly more in line with an isothermal radiative process.

Our excess fit gives a value of the phase fraction δp for the plasma to reach the EFR, which can be translated into a time $\delta t = 4.0 \pm 0.6$ d. With our value for the streaming velocity $v_{\rm strm}$ (assumed constant), this would make the distance from the apex at which the excess arises $d_{\rm EFR} = 7.6 \times 10^8$ km or 5.1 au. This value could be compared to simulations of colliding winds, taking into account adiabatic/radiative cooling of the CWR. However, we can also try to obtain a rough estimate by using a simpler analysis. The crucial parameter is χ (defined by Stevens et al. 1992). This gives the ratio of the cooling time-scale to the flow time-scale (roughly the time for the gas to flow a distance $d_{\rm sep}$ downstream), which indicates how radiative or adiabatic the wind–wind collision should be:

$$\chi \approx v_8^4 d_{12}/\dot{M}_{-7}. \quad (9)$$

Here, $v_8 = v/1000$ km s^{-1}, $d_{12} = d_{\rm sep}/10^{12}$cm and $\dot{M}_{-7} = \dot{M}/10^{-7}M_\odot$yr^{-1}.

We can substitute parameters for either the WR or O star as required. For WR 140, if we take $\eta = 0.0353$ from table 2 in Pittard & Dougherty (2006), then $\dot{M}$(WR) $= 3.3 \times 10^{-5}$M$_\odot$yr^{-1}. Using v_∞(WR) = 2860 km s^{-1} and $d_{\rm peri} = 1.59$ au ($d_{12} = 23.8$), then $\chi \approx 4.8$. So, the gas should flow downstream a distance of about $4.8 d_{\rm peri}$ before cooling (7.6 au). This is relatively close to the estimate in this paper (5.1 au). However, this it is probably fortuitous as there are many other factors that mean it should only be used as a rough guide: for example, the determination of χ in Stevens et al. (1992) assumes solar abundances – in reality, the WC7 gas will cool more quickly; clumping will also decrease the cooling time (at least within the clumps), but the clumps may be destroyed even faster (see Pittard 2007); gas colliding away from the lines of centre of the stars will be of lower density and will take longer to cool.

7 CONCLUSION

The 2009 periastron campaign on WR 140 provided increased accuracy on the orbital parameters, new estimates for the WR- and O-star masses and new constraints on the relative mass-loss rates. For this purpose, we have modified the geometrical model of Lührs (1997) in order to adapt it to an eccentric orbit. This new version of the model also gives an estimation of the distance of the EFR from the apex of the shock cone of about 5.1 au, which could be compared with hydro/radiative simulations of the wind–wind collision. The observational campaign is also a very encouraging success in terms of professional–amateur collaboration, and we hope this will give rise to similar initiatives in the future. A more sophisticated theoretical investigation should also be performed to confirm our results about the geometry of the shock cone. Meanwhile, the $\sim d^{-2}$ dependency of the excess, shown in Fig. 7, strongly suggests that some type of isothermal radiative process is involved here, rather than adiabatic, despite the large separation of the two stars even at periastron. Links with observations in other spectral domains (X-ray, infrared and radio) will certainly provide valuable clues about the physics. Finally, we have attempted to isolate the WR spectrum from the O-star spectrum from our data in order to identify the spectral type of the latter more precisely. Additional photometric and spectropolarimetric data obtained during the campaign will be presented in a future publication.

ACKNOWLEDGMENTS

RF is grateful to the whole Mons team and the other amateur astronomers who invested personal time and money in this project and contributed to its success. AFJM is grateful to NSERC (Canada) and FQRNT (Quebec) for financial assistance. ANC acknowledges support from Comité Mixto ESO-Gobierno de Chile and from the BASAL/FONDAP project. TM acknowledges financial support from Belspo for contract PRODEX-GAIA DPAC. JMP gratefully acknowledges support from the Royal Society. PMW is grateful to the Institute for Astronomy for hospitality and continued access to the facilities of the Royal Observatory, Edinburgh. We are grateful to the Instituto de Astrofísica de Canarias (IAC) and its staff for their support of the Mons project. We want to thank Professor Francisco Sanchez, Director of the IAC, and Dr Miquel Serra for assistance and the generous allotment of telescope time at Mons.

REFERENCES

Amôres E. B., Lépine J. R. D., 2005, AJ, 130, 659
Bagnulo S., Jehin E., Ledoux C., Cabanac R., Melo C., Gilmozzi R., the ESO Paranal Science Operations Team, 2003, The Messenger, 114, 10
Bartzakos P., Moffat A. F. J., Niemela V. S., 2001, MNRAS, 324, 33
Cantó J., Raga A. C., Wilkin F. P., 1996, ApJ, 469, 729
Conti P. S., Alschuler W. R., 1971, ApJ, 170, 325
Crowther P. A., De Marco O., Barlow M. J., 1998, MNRAS, 296, 367
Demers H., Moffat A. F. J., Marchenko S. V., Gayley K. G., Morel T., 2002, ApJ, 577, 409
Dougherty S. M., Beasley A. J., Claussen M. J., Zauderer B. A., Bolingbroke N. J., 2005, ApJ, 623, 447 (D05)
Eenens P. R. J., Williams P. M., 1994, MNRAS, 269, 1082
Hill G. M., Moffat A. F. J., St-Louis N., Bartzakos P., 2000, MNRAS, 318, 402
Hill G. M., Moffat A. F. J., St-Louis N., 2002, MNRAS, 335, 1069
Lührs S., 1997, PASP, 109, 504
Marchenko S. V. et al., 2003, ApJ, 596, 1295 (M03)
Markwardt C. B., 2009, in Bohlender D. A., Durand D., Dowler P., eds, ASP Conf. Ser. Vol. 411, Astronomical Data Analysis Software and Systems (ADASS) XVIII. Astron. Soc. Pac., San Francisco, p. 251
Martins F., Schaerer D., Hillier D. J., 2005, A&A, 436, 1049
Massey P., Valdes F., Barnes J., 1992, http://iraf.noao.edu/docs/spectra.html
Moffat A. F. J., St-Louis N., eds, 2002, ASP Conf. Ser. Vol. 260, Interacting Winds from Massive Stars. Astron. Soc. Pac., San Francisco
Moffat A. F. J., Lamontagne R., Williams P. M., Horn J., Seggewiss W., 1987, ApJ, 312, 807
Moffat A. F. J. et al., 1998, ApJ, 497, 896
Neiner C., de Batz B., Mekkas A., Cochard F., Martayan C., 2007, in Bouvier J., Chalabaev A., Charbonnel C., eds, SF2A-2007: Proc. Annual Meeting of La Société Franaise d'Astronomie et d'Astrophysique (Sf2A), The Be Star Spectra (BeSS) data base. Sf2A, France, p. 538
Pittard J. M., 2007, ApJ, 660, L141
Pittard J. M., Dougherty S. M., 2006, MNRAS, 372, 801
Plaskett J. S., 1924, Publications of the Dominion Astrophysical Observatory Victoria, 2, 287
Setia Gunawan D. Y. A., van der Hucht K. A., Williams P. M., Henrichs H. F., Kaper L., Stickland D. J., Wamsteker W., 2001, A&A, 376, 460
Smith L. F., Shara M. M., Moffat A. F. J., 1990, ApJ, 358, 229
Stevens I. R., Blondin J. M., Pollock A. M. T., 1992, ApJ, 386, 265
Torres A. V., Conti P. S., Massey P., 1986, ApJ, 300, 379
van der Hucht K. A., 2001, New Astron. Rev., 45, 135
Walborn N. R., Sota A., Maíz Apellániz J., Alfaro E. J., Morrell N. I., Barbá R. H., Arias J. I., Gamen R. C., 2010, ApJ, 711, L143
Williams P. M., van der Hucht K. A., van der Woerd H., Wamsteker W. M., Geballe T. R., 1987, in Lamers H. J. G. L. M., De Loore C. W. H., eds, Astrophys. Space Sci. Libr. Vol. 136, Instabilities in Luminous Early-Type Stars. Reidel, Dordrecht, p. 221

This paper has been typeset from a TEX/LATEX file prepared by the author.